

# Aerosol Optical Properties Measurement using the Orbiting High Spectral Resolution Lidar onboard DQ-1 Satellite: Retrieval and Validation

Chenxing Zha<sup>1</sup>, Lingbing Bu<sup>1</sup>, Zhi Li<sup>1,2</sup>, Qin Wang<sup>3</sup>, Ahmad Mubarak<sup>1</sup>, Pasindu Liyanage<sup>1</sup>, Jiqiao Liu<sup>4</sup>,  
5 Weibiao Chen<sup>4</sup>

<sup>1</sup>School of Atmospheric Physics, Nanjing University of Information Science and Technology, Nanjing, 210044, China

<sup>2</sup>Nanjing Movelaser Technology Co., Ltd, Nanjing, 210044, China

<sup>3</sup>Tianjin Meteorological Radar Research and Test Centre, Tianjin, 300061, China

<sup>4</sup>Key Laboratory of Space Laser Communication and Detection Technology, Shanghai Institute of Optics and Fine Mechanics,  
10 Chinese Academy of Sciences, Shanghai, 201800, China

*Correspondence to:* Lingbing Bu (001779@nuist.edu.cn), Qin Wang (18262602365@163.com)

## Abstract.

The Atmospheric Environment Monitoring Satellite (AEMS), also called DaQi-1 (DQ-1), was launched in April 2022, one of  
its main payloads is the High Spectral Resolution Lidar (HSRL) system. This new system enables the accurate measurements  
15 of global aerosol optical properties, which can be used in Geo-scientific community after the Cloud-Aerosol Lidar and Infrared  
Pathfinder Satellite Observation (CALIPSO) retirement. Developing a suitable retrieval algorithm and validating retrieved  
results are necessary. This research demonstrates a retrieval algorithm for aerosol optical properties using the DQ-1 HSRL  
system. This method has retrieved the aerosol linear depolarization ratio, backscatter coefficient, extinction coefficient, and  
optical depth. For validation purposes, we compared retrieved results with those obtained through CALIPSO. The results  
20 indicate that the profiles of the two datasets are in good agreement, with DQ-1 showing an improved signal-to-noise ratio  
(SNR). Optical property profiles from National Aeronautics and Space Administration (NASA) Micro Pulse Lidar Network  
(MPLNET) stations were selected for validation with the DQ-1 measurements, resulting in a relative error of 25%. Between  
June 2022 and December 2022, aerosol optical depth measurements using the DQ-1 satellite and the AERosol RObotic  
NETWORK (AERONET) were correlated and yielded a value of  $R^2$  equal to 0.803. We use the DQ-1 dataset to initially  
25 investigate the transport processes of the Saharan dust and the South Atlantic volcanic aerosols. These validations and  
applications show that the DQ-1 HSRL system can accurately measure global aerosols and holds significant prospects for earth  
science applications.

**Keywords:** Aerosol Optical Parameters; Spaceborne High Spectral Resolution Lidar; Validation.

## 1 Introduction

30 Aerosols are tiny solid and liquid particles suspended in the atmosphere, an atmospheric aerosol particle typically ranges from 0.01 to 10  $\mu\text{m}$  in diameter. The earth's radiation balance is influenced by aerosol's capability to scatter and absorb radiation. Similarly, as cloud condensation nuclei, aerosols influence cloud formation and affect global climate change (Kaufman et al., 2002). The aerosol optical properties can be used to study the above scientific problems. Lidar, as an active remote sensing instrument, can obtain aerosol optical parameters at a high spatial and temporal resolution. Based on the various observation  
35 approaches, lidar can be divided into ground-based lidar, airborne lidar, and spaceborne lidar. Typical examples of ground-based Lidar include the European Aerosol Research Lidar NETwork (EARLINET) (Pappalardo et al., 2014; Guibert et al., 2005), the Micro-Pulsed Lidar (MPL) network (Welton et al., 2001), The Asian Dust and Aerosol Lidar Observation Network (AD-Net) (Nishizawa et al., 2016), etc. There are several advantages of ground-based lidar: easy maintenance of the instrument, and long-term stable observation of specific areas. The life cycle and evolution process of aerosols can be studied through  
40 ground-based lidar systems. Furthermore, it is beneficial to validate spaceborne and airborne measurements with ground-based lidar systems (Pitari et al., 2013; Mattis et al., 2004). The disadvantage of ground-based observation includes limited spatial coverage capability, which makes it impossible to carry out large-scale continuous observation. The airborne lidar system enables extensive and continuous observations over a wide range, thereby compensating for the limitations associated with ground-based systems. Typical examples of airborne Lidar include the NASA Langley airborne High Spectral Resolution  
45 Lidar (HSRL-1) and the Langley airborne High Spectral Resolution Lidar - Generation 2 (HSRL-2). The two airborne lidar experiments were conducted to observe aerosol optical properties quantitatively and to investigate the impact of aerosols on radiation, clouds, and air quality (Knobelspiesse et al., 2011; Burton et al., 2012a; Burton et al., 2012b). The German Aerospace Center (DLR) has also developed an airborne HSRL system to measure aerosol optical properties and types (Esselborn et al., 2008; Groß et al., 2013). The Shanghai Institute of Optics and Fine Mechanics (SIOM) of the Chinese Academy of Sciences,  
50 in collaboration with Nanjing University of Information Science and Technology (NUIST), Zhejiang University (ZJU), and other institutions, has conducted observational experiments on airborne HSRL system at two distinct geographical locations, Dunhuang and Shanhaiguan. This airborne system is a scaled system of the DQ-1 HSRL. The aerosol optical parameters in these two regions obtained by the HSRL system were validated using CALIPSO, ground based MPLNET, and sun photometer. An analysis was conducted on the sources, sinks, and types of aerosols in the local area (Wang et al., 2020; Xu et al., 2020;  
55 Zhu et al., 2021; Juxin et al., 2023; Changzhe et al., 2023). The airborne lidar system addresses the shortcomings of ground-based observations. Nevertheless, the system's observations are limited by factors such as flight paths and meteorological conditions to prevent prolonged data collection, unable to provide long-term observations, and low spatiotemporal resolution making it impossible to observe the microscale system.

Global information about aerosol optical parameters is vital to familiarizing with aerosol sources and sinks. This global  
60 information is valuable for tracking aerosol particle dispersion pathways and compensates for the limitations of ground-based and airborne observations. Although satellite observations have the drawbacks of low temporal and spatial resolution, as well

as long revisit period, they can obtain global aerosol optical parameters (Qin et al., 2016; Huang et al., 2008). With space technology's advancement, several spaceborne lidar systems have been developed. The Cloud-Aerosol Lidar and Infrared Pathfinder Satellite Observation (CALIPSO), developed by NASA, is the most representative spaceborne lidar satellite. Since its launch in 2006, it has been fully verified by comparing its dataset with other multi-source datasets (Bibi et al., 2015; Wang et al., 2016; McGill et al., 2007; Chiang et al., 2011). Investigation and discrimination of clouds and aerosols, optical properties, types, and microphysical characteristics of the aerosol were performed. An advanced-level retrieval algorithm was developed, to present an outstanding contribution to research on the optical properties and spatiotemporal distribution of aerosols globally (Getzewich et al., 2018; Vaughan et al., 2019; Winker et al., 2010; Liu et al., 2019b). Due to insufficient power (Langley Research Center, 2024), the CALIPSO science mission ended in August 2023, a well-established and developed new-generation spaceborne Lidar is needed to replace CALIPSO for global aerosol observation. As a new-generation lidar, high spectral resolution lidar filters out the Mie scattering in the return signals through a filter. This method avoids the assumptions made by traditional lidar during retrieval, resulting in more precise results (Hair et al., 2001). NASA has developed the Cloud-Aerosol Transport System (CATS) as a low-cost payload for the International Space Station (ISS). The system design incorporates a high spectral resolution lidar and elastic backscattering lidar. It has unveiled the characteristics of aerosols and clouds and their interactions. Similarly, it has conducted in-depth scientific observations in certain areas (Xiong et al., 2023; Proestakis et al., 2019; Yorks et al., 2016). In addition, the Atmospheric Laser Doppler Instrument (ALADIN) lidar loaded on the AEOLUS provides results of global aerosol optical parameters retrieved by L2A data which had performed the comparison with the ground-based lidar product (Abril-Gago et al., 2022). Furthermore, under the leadership of NASA, the Atmosphere Observing System (AOS) international program analyzes the additional value provided by a spaceborne HSRL system. This research has shown that the results of spaceborne HSRL systems are more accurate than the results of traditional elastic backscatter lidar in three different cases (Cornut et al., 2023). ESA and JAXA collaborated on the development of Earth Cloud, Aerosol and Radiation Explorer (EarthCARE), equipped with an ATmospheric LIDar (ATLID). The primary objective of this mission is to observe and characterize clouds and aerosols, as well as to measure the infrared radiation emitted from the Earth's surface and the solar radiation reflected from the atmosphere. This satellite is anticipated to be launched in the spring of 2024 (Reverdy et al., 2015; Wehr et al., 2023). It is worth noting that the above new spaceborne lidar satellites are in the planning stage and have not actually been launched. The previous observing satellites have stopped working, and now global aerosol data, based on spaceborne lidar, is facing a gap.

China launched the Atmospheric Environment Monitoring Satellite (AMES), also called DaQi-1 (DQ-1), from the Taiyuan Satellite Launch Center on April 16, 2022. The main payload is the Aerosol and Carbon Detection Lidar (ACDL), which includes a dual-polarization HSRL system based on an iodine vapor filter (Liu et al., 2019a; Zheng et al., 2020; Dong et al., 2019). Prior to the launch of DQ-1, an airborne scaling system for ACDL was developed, deployed, and tested at two sites: Shanhaiguan and Dunhuang. The results ensure the feasibility of the scaling system and verify the accuracy of the observations (Wang et al., 2020; Xu et al., 2020; Zhu et al., 2021; Juxin et al., 2023; Changzhe et al., 2023). The successful operation of the airborne scaling system indicates accurate design and observation of DQ-1 system and provides a foundation for spaceborne

retrieval algorithm. After the above operation, The DQ-1 satellite was launched into a 705-kilometer orbit. Now, DQ-1 must establish a robust retrieval algorithm and conduct multi-source data validation on algorithmic outcomes, ensuring the system observation's precision.

100 In this work, we studied the aerosol optical parameter retrieval algorithm of the spaceborne HSRL system. This algorithm has used the data of the attenuated backscatter coefficient of the perpendicular polarized channel, parallel polarized channel, and molecular scattering channel of the DQ-1 ACDL system. We used the atmospheric temperature and pressure data in the Medium-Range Weather Forecasts Reanalysis v5 (ERA5) to calculate the molecular backscatter coefficient. The attenuated backscatter coefficient is first compared with the CALIPSO data set to ensure the accuracy of instrument calibration. The retrieval results were then compared with the corresponding data products of CALIPSO and NASA MPLNET qualitatively. 105 To ensure the accuracy, the retrieved aerosol optical depth was against the corresponding data products of AERONET where the errors were analyzed. The comparison results confirm the accuracy of DQ-1 L2A datasets and retrieval algorithm. Lastly, We use data from DQ-1 to analyze the transport processes of Saharan dust and South Atlantic tropospheric volcanic aerosol. This primary application area discloses the scientific significance of the high-performance system introduced by the DQ-1 satellite in the context of global aerosol detection applications, rendering it an alternative approach to the CALIPSO satellite.

## 110 **2 Instrumentation and method**

### **2.1 DQ-1 ACDL system**

#### **2.1.1 System overview**

The ACDL system includes a Integral Path Differential Absorption (IPDA) lidar system and a High Spectrum Resolution Lidar (HSRL) system, capable of performing integrated satellite-based detection of atmospheric aerosols, clouds, and carbon dioxide (Weibiao et al., 2023). The main parameters of the DQ-1 HSRL system are shown in Table 1. The laser beam of the HSRL system has a wavelength of 532.245 nm, a pulse repetition frequency of 40 Hz, and the absorption line of iodine molecules corresponds to line 1110 (Weibiao et al., 2023). The laser produces two distinct pulses, pulse A and pulse B, to observe the atmosphere practically, both of the pulses are normalized prior to the retrieval process. The laser beam is off-zenith, pointing at an angle of 2 degree and remains steady due to the attitude control system. The optical system has a 120 Cassegrain-type telescope with a primary mirror of 1-meter diameter. The receiving system consists of three optical channels: the perpendicular polarized channel, the parallel polarized channel, and the high spectral resolution channel (Weibiao et al., 2023; Dai et al., 2023). The parallel and perpendicular channels serve the function of obtaining polarization information of the aerosol, a Polarizing Beam Splitter (PBS) is placed to reduce polarization cross talk. To verify the accuracy of the parallel and perpendicular channels, we retrieved the depolarization ratio of atmospheric molecules at high 125 altitude. The results, shown in Figure 1, indicate that the depolarization ratio is 0.5%, which confirms the accuracy of the two optical channels. The high spectral resolution channels function to separate Mie scattering and Rayleigh scattering in the

signal, obtaining the molecular scattering profile. The measured absorption spectrum lines of the iodine vapor filter on ACDL are shown in Figure 2a. The principle of aerosol scattering suppression by the iodine filter is also shown in Figure 2a, based on the characteristic of aerosol Mie scattering spectra having a narrow bandwidth compared to molecular Rayleigh scattering, to get rid of aerosol scattering efficiently. Based on the previous simulation, the most suitable temperature, pressure and length of the iodine filter were selected, resulting in a suppression ratio of 25 dB (Dong et al., 2018), this suppression ratio is sufficient to filter out the Mie scattering for subsequent retrieval. Figure 2b shows the comparison of signals before and after filtering, with no significant aerosol Mie scattering signal in the filtered signal, presenting a residual portion of molecular Rayleigh scattering. The detector output signals obtained at three channels make up the L2A attenuated backscatter coefficients used in the retrieval algorithm.

### 2.1.2 Retrieval algorithm

Prior to L2A data retrieval, some pre-processing steps are taken, including SNR control, moving average, and pulse averaging. SNR control refers to removing the backscatter signal with insufficient SNR, this includes removing the heavy cloud-covered signal, and removing erroneous echoes under the surface and signals with poor SNRs, this is achieved by setting an SNR threshold. The threshold is determined by the magnitude of the weak echo signal beneath the dense cloud cover. After this, the low-pass filtering algorithm is used to perform moving average on the profile. To achieve the design's horizontal resolution of 20 km, the profiles within a 20 km horizontal range are normalized and averaged. There is an energy difference between laser pulses A and B, where the L2A data have been calibrated during the production, and the time delay of pulses A and B is 200  $\mu$ s. To improve the SNR of the raw data, the two pulses have been normalized and averaged. The main retrieval processes are presented through a flowchart, as shown in Figure 3. The ERA5 and DQ-1 L2A datasets are given, which serve as the algorithm's initial point. The ERA5 temperature and pressure data corresponding to the DQ-1 satellite is incorporated into the atmospheric model (Tenti et al., 1974) to compute molecular backscattering spectra. Subsequently, to determine the transmittance of the molecules,  $T_m$ , the spectra is convolved with iodine absorption spectra. The computation of the volume depolarization ratio employs data from both parallel and perpendicular depolarized channels, while the backscatter coefficient is from three channels and  $T_m$ . The extinction coefficient is computed from parallel and high spectral resolution channels, along with  $T_m$ . The specific mathematical equations are presented as follows.

Based on the mentioned receiving system principles outlined in Section 2.1.1, the equations for the attenuated backscatter coefficient are described as follows, with a perpendicular depolarized channel, parallel depolarized channel, and high spectral resolution channel.

$$B^\perp(r) = \frac{P(r)r^2}{P_0\eta^\perp AL} [\beta_m^\perp(r) + \beta_a^\perp(r)] \times \exp \left\{ -2 \int_0^r [\alpha_m(r) + \alpha_a(r)] dr \right\} \quad (2.1)$$

$$B_C^\parallel(r) = \frac{P(r)r^2}{P_0\eta_C^\parallel AL} [\beta_m^\parallel(r) + \beta_a^\parallel(r)] \times \exp \left\{ -2 \int_0^r [\alpha_m(r) + \alpha_a(r)] dr \right\} \quad (2.2)$$

$$B_H^{\parallel}(r) = \frac{P(r)r^2}{P_0\eta_H^{\parallel}AL} [T_m(r)\beta_m^{\parallel}(r) + T_a(r)\beta_a^{\parallel}(r)] \times \exp \left\{ -2 \int_0^r [\alpha_m(r) + \alpha_a(r)] dr \right\} \quad (2.3)$$

In Eqs. (2.1) ~ (2.3), the symbols  $\perp$  and  $\parallel$  represent signals characterized by perpendicular polarized and parallel polarized, respectively. The ratio between them reflects the sphericity of the target. The subscripts  $C$  and  $H$  represent the signals of the parallel channel and the high spectral resolution channel, with their ratio reflecting the proportion of aerosol Mie scattering signals to the backscattering signals.  $P(r)$  represents the power of the laser echo signal at distance  $r$ .  $P_0$  represents the emitting power of the laser,  $\eta$  represents the optical efficiency of the corresponding receiving channel,  $A$  represents the aperture of the telescope, and  $L$  stands for the half of the pulse spatial transfer length, where  $L$  is calculated as  $L = c\Delta t/2$ , with  $c$  representing the speed of light and  $\Delta t$  denoting the pulse duration. System correction has been implemented to ensure that the data is solely contingent upon atmospheric conditions.  $\beta_m(r)$  and  $\beta_a(r)$  represents the backscatter coefficient of molecules and aerosols respectively,  $\alpha_m(r)$  and  $\alpha_a(r)$  represents the molecular and the aerosol extinction coefficients. The molecular backscatter coefficient and extinction coefficient are calculated by the S6 molecular model (Tenti et al., 1974) using the data of temperature and pressure provided by ERA5.  $T_m(T, p)$  and  $T_a(T, p)$  respectively represents the transmittance of the echo signal of molecular and aerosol while passing the iodine filter, they can be expressed as:

$$T_m(T, p) = \int F(v) \int R_m(v', T, p) l(v - v') dv' dv \quad (2.4)$$

$$T_a(T, p) = \int F(v) \int R_a(v', T, p) l(v - v') dv' dv \quad (2.5)$$

Where  $l(v - v')$  represents the spectrum distribution of the laser beam,  $F(v)$  represents the normalized transmission spectrum of the iodine filter.  $R_m(v', T, p)$  represents the normalized molecular scattering spectrum related to temperature and pressure.  $R_a(v', T, p)$  represents the normalized aerosol particles scattering spectrum (Dong et al., 2018). To ensure the stability of the transmittance spectrum, the temperature and pressure of iodine in the filter are strictly controlled on the orbit.

Simultaneous Eqs. (2.1) ~ (2.5), calculate the aerosol backscatter coefficient as follows:

$$\beta_a(r) = \beta_m(r) \frac{[1 + \delta(r)] [T_m(r) - T_a(r)] K(r)}{(1 + \delta_m(r)) [1 - T_a(r) K(r)]} - \beta_m(r), \quad (Xu et al., 2020) \quad (2.6)$$

Where  $\delta_m$  represents the depolarization ratio of molecules, and  $\delta(r)$  represents the depolarization ratio, which is dependent to the spherical state of the target.  $K(r_0)$  is the ratio of parallel channel to molecular channel, it can be expressed as:

$$K(r_0) = \frac{B_C^{\parallel}(r_0)}{B_H^{\parallel}(r_0)} \quad (2.7)$$

The particulate depolarization ratio is expressed as:

$$\delta_p(r) = \frac{\beta_m(r)[\delta(r) - \delta_m(r)] + \beta_a(r)\delta(r)[1 + \delta_m(r)]}{\beta_m(r)[\delta_m(r) - \delta(r)] + \beta_a(r)[1 + \delta_m(r)]}, \quad (Tesche et al., 2009) \quad (2.8)$$

Simultaneous Eqs. (2.1) ~ (2.5), the atmospheric optical depth is defined as:

$$\tau(r_0) = \int_0^{r_0} (\alpha_a(r) + \alpha_m(r)) dr = -\frac{1}{2} \ln \left[ \frac{(1 - K(r_0)T_a(r_0))(1 + \delta_m)B_H^{\parallel}}{(T_m(r_0) - T_a(r_0))} \right], \quad (Xu et al., 2020) \quad (2.9)$$

Differentiating the Eq. (2.9), the aerosol extinction coefficient can be expressed as:

$$\alpha_a(r_0) = \frac{\partial \tau(r_0)}{\partial r} - \alpha_m(r_0) = -\frac{1}{2} \frac{\partial}{\partial r} \left\{ \ln \left[ \frac{(1 - K(r_0)T_a(r_0))(1 + \delta_m)B_H^{\parallel}}{(T_m(r_0) - T_a(r_0))} \right] \right\} - \alpha_m(r_0), \text{ (Xu et al., 2020)} \quad (2.10)$$

The aerosol lidar ratio is expressed as:

$$S_a(r) = \frac{\alpha_a(r)}{\beta_a(r)} \quad (2.11)$$

## 2.2 CALIPSO

190 The Cloud-Aerosol Lidar and Infrared Pathfinder Satellite Observation (CALIPSO) satellite, launched on April 28, 2006, is equipped with the Cloud-Aerosol Lidar with Orthogonal Polarization (CALIOP) instrument operating at a wavelength of 532 nm and 1064 nm. CALIOP continuously observes the Earth's atmosphere to monitor attenuated backscatter data with depolarization and color ratios. The CALIPSO Level 2 data includes vertical profiles of aerosol backscatter coefficient, extinction coefficient, and depolarization ratio. Various approved methodologies have been deployed to accurately monitor and observe the Earth's atmosphere (Mcpherson et al., 2010). The retrieval algorithm employed for Level 2 data processing has been refined frequently, with the updated version of V4.51. Due to insufficient power supply, the CALIPSO science mission has ended on August 1, 2023, demanding the deployment of a new satellite platform to continue global observations of clouds and aerosols.

## 2.3 AERONET

200 The AEROSOL ROBOTIC NETWORK (AERONET) is a ground-based aerosol remote sensing network established by the mutual collaboration of NASA and LOA-PHOTONS (CNRS) (Holben et al., 1998). At the moment, this global automated observation network has coverage in major regions throughout the world. The network utilizes the automated sun photometers produced by Cimel Electronique as the primary instrument to observe the atmosphere. The instruments at most sites collect data daily, which is then further processed by the instrumental setup. AERONET provides a valuable resource for multi-wavelength, continuous, and accurate aerosol optical depth data products. These data products play a significant role in studying global aerosol transport, aerosol radiative effects, validating radiative transfer models, and verifying satellite-based aerosol remote sensing results.

## 2.4 NASA MPLNET

210 The NASA Micro-Pulse Lidar Network (MPLNET) is a globally distributed network equipped with a polarized Micro-Pulse Lidar (MPL) system that has been operating continuously since 2000 (Welton et al., 2001). With more than 70 well-established observational stations worldwide, MPLNET has several underlying surface conditions, allowing it to collect ongoing aerosol vertical profiles in different regions. The aerosol backscatter coefficient, extinction coefficient, and depolarization ratio can be measured by its system. Most of the MPLNET sites are strategically situated near the observation sites of the AERONET. The

integration of MPLNET and AERONET is used to make a potential approach possible, and to facilitate the robust validation  
215 of satellite instruments and other scientific objects.

## 2.5 HYSPLIT model

The NOAA Hybrid Single Particle Lagrangian Integrated Trajectory (HYSPLIT) model is a widely used atmospheric transport and dispersion model developed by the National Oceanic and Atmospheric Administration (NOAA) (Draxler and Hess, 1997; Stein et al., 2015) . It has been extensively employed for various applications, including air pollution studies, atmospheric  
220 research, emergency response planning, and radiological assessments. The HYSPLIT model employs a Lagrangian approach to trace aerosol movement and simulate the dispersion of pollutants or other atmospheric constituents over time. This model provides valuable insight into the long-range transport of pollutants, the dispersion patterns of hazardous substances, and the understanding of atmospheric dynamics on local, regional, and global scales (Crawford et al., 2016; Wang and Chen, 2014).

## 3 Validation of retrieval result

### 225 3.1 Validation with CALIPSO

We conducted a comparative validation between the CALIPSO and DQ-1 satellites on a closely aligned orbit on June 6, 2022. The ground tracks of both satellites are illustrated in Fig. 4. The two satellites follow orbital trajectories extending from the Central Asian region across the Arabian Peninsula to the open ocean south of Africa, with a spatial separation of 400 km and a temporal difference of 60 minutes. In order to verify the consistency of the raw data, Figures 5a and 5b describe the total  
230 attenuated backscatter coefficients of DQ-1 and CALIPSO. Within the geographical area of 40°N to 10°N, at an altitude below 5 km, desert dust aerosols were investigated in large proportion. The attenuated backscatter coefficient in this area falls within the range of  $10^{-3}$  to  $10^{-2}$   $\text{km}^{-1}\text{sr}^{-1}$ . This geographical area intersects the Arabian Peninsula and the Iranian Plateau. At an altitude of 15 km, the distribution of cirrus was observed, with the laser return signal failing to penetrate certain portions of the cloud cover. South of 10°N, as the two satellites entered the maritime region, there was no observed aerosol distribution. The cumulus  
235 clouds were distributed at an altitude of 3 km, and some mid-level clouds reached an altitude of 5 km. South of 20°N, at an altitude higher than 20 km, DQ-1 observed the distribution of stratospheric volcanic aerosols. Due to the impact of temporal and spatial inconsistencies, the results obtained about cloud detection from CALIPSO and DQ-1 have dissimilarities. Nevertheless, both the aerosol results exhibit similar trends, with numerical values ranging from  $10^{-3}$  to  $10^{-2}$   $\text{km}^{-1}\text{sr}^{-1}$ . To further evaluate the differences of both the raw signals. Figure 5e presents the average raw signal with a latitude ranging from 20°N  
240 to 22°N, having molecular backscatter coefficient calculated from ERA5 temperature and pressure data for analysis. The raw signals of the DQ-1 and the CALIPSO align with the molecular scattering profile. The local variations in the high-altitude atmosphere are relatively small, making system noise more easily distinguishable. Using high-altitude echo signals as noise and utilizing the ratio of the noise to echo signals as SNR. To compare both the signal quality, the SNR of the total attenuated backscattered signals was analyzed, as illustrated in Figures 5c and 5d. The vertical resolution of the DQ-1 attenuated



245 backscatter coefficient is 48 m, while CALIPSO exhibited a vertical resolution of 30 m below 8 km and 60 m between 8 km and 20 km. In areas with aerosol distribution, the value of CALIPSO's signal SNR varied from 10 to 40, and the SNR of DQ-1's signal exceeded 40. Additionally, DQ-1 has maintained a high-altitude molecular scattering SNR above 20, whereas CALIPSO's high-altitude molecular scattering signal SNR has a value of less than 20. In conclusion, the two satellites give consistent raw data results in close orbits, DQ-1 operating at a higher resolution, achieving a better SNR.

250 Figure 6 shows a comparative analysis of the retrieval results obtained from both systems. Figures 6a and 6b show the latitudinal distribution of aerosol extinction coefficients with a  $10^{-1} \text{ km}^{-1}$  value. Figures 6c and 6d illustrate the latitudinal distribution of backscatter coefficients for both systems, with a value of  $10^{-2} \text{ km}^{-1}\text{sr}^{-1}$ . Due to spatial differences, the results of high-level clouds obtained by the two systems are different. Furthermore, at a height below 2 km in the lower troposphere, at a spanning of  $5^{\circ}\text{N}$  to  $15^{\circ}\text{N}$ , CALIPSO has obtained significantly higher retrieval values, discriminating the aerosol types. In

255 Figures 6j and 6k, we chose two satellites for the profile comparison of the aerosol extinction coefficient and backscatter coefficient at a latitude of  $22^{\circ}\text{N}$ . The backscatter coefficient was retrieved from both satellites with a value of  $10^{-3} \text{ km}^{-1}\text{sr}^{-1}$  at a height lower than 4 km, whereas the aerosol extinction coefficient was retrieved with a  $10^{-1} \text{ km}^{-1}$  value. This indicates a relatively dense distribution of aerosols. Besides atmospheric variations caused by specific spatiotemporal effects, both variable's trends and numerical distributions are closely related. Figures 6e, 6f and 6i depicts the particulate depolarization

260 ratio. The value of depolarization ratio at low altitude obtained from DQ-1 is 0.3, demonstrating the nature of dust. Similarly, the depolarization ratio of clouds at a high altitude of 15 km measures a value of 0.4, presents the characteristics of cirrus clouds composed of ice crystals. The retrieval results of the particulate depolarization ratio from CALIPSO exhibit a mean value of 0.3, which is consistent with DQ-1. Figures 6g and 6h depict the latitudinal distribution of aerosol lidar ratio. The advantage of the DQ-1 HSRL system is that it can retrieve the lidar ratio without assumptions, which is significantly different

265 from CALIPSO. DQ-1 indicates that the lidar ratio of aerosol particles is around 40 sr, describing the characteristics of dust, consistent with Calipso's aerosol type. For cirrus at altitude of 10 to 15 km, the retrieved lidar ratio of DQ-1 is less than 40 sr, indicating the characteristics of ice crystals. Due to the proximity of the CALIPSO orbit to oceanic regions, below 3 km altitude and south of  $18^{\circ}\text{N}$ , CALIPSO identified sea salt aerosols, with numerical values representing a lidar ratio of 20 sr and retrieved a depolarization ratio less than 0.1. Considering the spatiotemporal between the two satellites, the retrieval results of DQ-1

270 and CALIPSO are consistent. DQ-1, operating at high-resolution conditions, achieves a high signal-to-noise ratio and presents reliable retrieval results.

### 3.2 Validation with MPLNET

We qualitatively compared the aerosol optical parameter data products from the NASA MPLNET ground station with the retrieval results of DQ-1. This comparison has three surface types: land, ocean, and coastal regions. Profile-averaged findings

275 inside a circle with a radius of 100 kilometers, centered on MPLNET stations, were explicitly chosen for DQ-1 data. For MPLNET data, we utilized the average MPLNET profile within 15 minutes of DQ-1 transit. Figure 7 illustrates the validation results. The change in lower atmospheric aerosols is fast and characterized by high local heterogeneity, whereas the SNR at a

high altitude is comparatively low. Hence, we selected the data at an altitude range of 1 km to 8 km for comparison. Three selected distinct surface types, namely, land, coastal, and oceanic regions, correspond to the Apalachin, El Arenosillo, and Santa Cruz Tenerife sites. The location of these three sites and the satellite trajectory are illustrated in Figures 7c, 7f, and 7i. The difference between the satellite and ground-based retrieval results is quantified, as shown in Figure 8.

The Apalachin site is inland in the United States, where satellite passes during nighttime hours. At this site, aerosol backscatter coefficients obtained from satellites and ground-based observations exhibit a relatively good correspondence at an altitude range of 3 km to 5 km. The relative discrepancy between the two observations is less than 25% within this range. However, below 3 km, the measurements are influenced by clouds, increasing the error between the two datasets. Both satellite and ground-based observations indicate a decreasing trend in the backscatter coefficient with an altitude of more than 5 km. Above 5 km, ground-based data exhibit rapid variations, leading to increased variations between the two datasets. Below an altitude of 3 km, the depolarization ratio of the two remains consistent. Above 5 km, there is a difference in the depolarization ratio results obtained by the two observation platforms due to the influence of clouds. The El Arenosillo site is situated along the southwestern coast of Spain, and the profile comparison results are depicted in Figures 7d and 7e. Both observational methods indicate that the aerosol distribution exhibits relatively low variation within the altitude of 1 km to 6 km. Above 6 km, there is a decline in aerosol concentration with increasing altitude. The distribution of aerosol backscatter and depolarization ratio is consistent. The relative error between the two results is less than 25% at an altitudes above 2.5 km. The Santa Cruz Tenerife station is situated in the Canary Islands, northwest of Africa, near the ocean. The profiles of aerosol optical parameters from both satellite and ground-based results remain relatively consistent. The depolarization ratio and backscatter coefficient profiles from both sources exhibit a high degree of agreement when accounting for spatial disparities. The relative errors between the two results are less than 25%. Comparative analysis of NASA MPL ground-based data products, when there is no influence of cloud, reveals that the relative errors in aerosol extinction and backscatter coefficients between the two sources are about 25%. This further validates the DQ-1 satellite retrieval algorithm.

### 3.3 Validation with AERONET

Figure 9 illustrates a scatterplot comparison between aerosol optical depth data obtained from DQ-1 and AERONET Level 2.0 from June to December 2022. The DQ-1 data represents the average aerosol optical depth within a circular region of a radius of 100 km, centered on AERONET sites, derived through the retrieval process. The data from AERONET stations represent ground-based measurements obtained within a 15-minute time window when DQ-1 passes over these sites. The difference in elevation between the sub-satellite point and the AERONET station can introduce errors (Omar et al., 2013). To mitigate such errors, we excluded the deviated results at more than 200 meters from the station's altitude on the ground. To exclude cloud signals, we subject the DQ-1 aerosol optical depth data to cloud signal removal using the backscatter ratio for better quality enhancement. When the backscatter ratio exceeds 10, we consider it to indicate cloud signal, which is excluded from calculating aerosol optical depth (Ke et al., 2022). Aerosol optical depth measurements at a wavelength of 532 nm were missing at some AERONET stations. Hence, we employed data at a wavelength range of 500 nm to 550 nm as a substitute.

The results obtained from a first-order polynomial regression analysis of the scatterplot data revealed a variance of 0.803 and a root mean square error (RMSE) of 0.1231. Considering the spatiotemporal differences between the two datasets, the satellite-based and ground-based observations exhibited a commendable level of agreement. There are specific data points deviating from the fitted regression line. These deviating data points share a common characteristic: satellite-based data tends to exhibit higher values. This difference can be attributed to the incomplete removal of cloud signals during retrieval. Such issues have also been highlighted in prior studies (Omar et al., 2013). Due to the current status of DQ-1's Level 2A data processing, completed only from June to December 2022, and ongoing data processing efforts for specific AERONET datasets, the available quantity of matching results is limited. Further validation through satellite-ground comparisons over an extended period can be pursued.

## 320 **4 Preliminary application of retrieval result**

After validation with various well-established observational platforms, our research has provided initial verification of the observational accuracy of the DQ-1 HSRL system. The following work will showcase some of the scientific applications that can be achieved with DQ-1, unveiling the immense potential and scientific value of the high-performance system carried by this satellite in comprehensive atmospheric environmental monitoring.

### 325 **4.1 Observation of aerosol transport in East Africa**

In July 2022, DQ-1 observed the propagation of Saharan dust from the northeastern Sahara region of Africa towards the Atlantic region. The optical parameters along the aerosol transport path from 3<sup>rd</sup> July to 8<sup>th</sup> July were retrieved. Additionally, a six-day backward trajectory analysis using the NOAA HYSPLIT Model was conducted on July 8<sup>th</sup> over the northeastern Atlantic off the coast of South America. Within this six-day duration, the dust covers a distance of 4000 km, with an average speed of 30 km/h. These results are presented in Figure 10. From July 3<sup>rd</sup> to July 4<sup>th</sup>, DQ-1 observed a top height of 8 km for the aerosol layer, with the backscatter coefficient ranging from  $10^{-2}$  to  $10^{-1}$   $\text{km}^{-1}\text{sr}^{-1}$ . Following a westward transport over two days, July 7<sup>th</sup> to July 8<sup>th</sup>, the altitude distribution is reduced to 4 km, and the backscatter coefficient has fallen below  $10^{-2}$   $\text{km}^{-1}\text{sr}^{-1}$ . During this transport process, there was an observable trend of aerosol settling over the ocean, reducing the altitude distribution range and backscatter coefficient. Figures 10c and 10e show the lidar and particulate depolarization ratios, respectively. On July 3<sup>rd</sup>, measurements over West Africa indicated a lidar ratio distribution centered around 50 sr and the particulate depolarization ratio values within the range of 0.25 to 0.4, representing dust (Burton et al., 2012a; Groß et al., 2011; Groß et al., 2013). During the transport process, the value of the lidar ratio was constant at 50 sr, while the particulate depolarization ratio was reduced from 0.25 to 0.15. On July 8<sup>th</sup> measurements, the lidar ratio from the surface to 2 km altitude exhibited values centered around 20 sr, describing the characteristic of sea salt (Burton et al., 2012a; Groß et al., 2011; Groß et al., 2013). Above 2 km, the lidar ratio is about 50 sr, indicating a consistent presence of dust. These observations have revealed a stratified distribution of aerosols in this region. The satellite-based retrieval results have presented the spatial

variations in dust's position and optical properties during their transport. DQ-1 observed that as these aerosols were transported, their altitude, backscatter coefficient, and particulate depolarization ratio decreased at the lidar ratio's constant value.

#### 4.2 Observation of stratospheric aerosol distribution over the south Atlantic

345 From January 14<sup>th</sup> to 15<sup>th</sup>, 2022, the Tonga volcano experienced two significant eruptions, releasing a substantial volume of volcanic ash, gases, and water vapor into the upper atmosphere, forming extensive cloud formations. The volcanic ash reached an altitude of 20 km (Yufeng et al., 2022). DQ-1 observations over the South Atlantic have revealed various effects and distribution of volcanic aerosol in the stratosphere. As DQ-1 data is available from June to December 2022, we substituted data from February to June 2022 with CALIPSO data. Figure 11 presents the observed attenuated backscatter coefficient from  
350 January to December 2022 within the stratosphere over the South Atlantic Ocean, using both CALIPSO and DQ-1. The area in the figure, ranging from 20° S to 30° S, falls within CALIPSO's South Atlantic Anomaly (SAA) region. The laser energy is weaker in this region, resulting in a low SNR. On January 1<sup>st</sup>, CALIPSO detected no aerosol distribution within the stratosphere. Following a volcanic eruption in mid-January, on February 1<sup>st</sup>, significant signals emerged at an altitude of 20 km, with attenuated backscatter coefficients reaching  $10^{-3} \text{ km}^{-1}\text{sr}^{-1}$ . From February to June, stratospheric aerosols' distribution gradually  
355 extended from 5° S to 20° S latitude, with the attenuated backscattering reducing constantly to less than  $10^{-4} \text{ km}^{-1}\text{sr}^{-1}$ . By May 1<sup>st</sup>, due to insufficient laser energy, CALIPSO received weak volcanic aerosol backscatter signals, making them difficult to distinguish from system noise. By June 1<sup>st</sup>, DQ-1 initiated observations in this region, revealing the presence of stratospheric aerosols at an altitude of more than 20 km, spanning from 0° S to 40° S latitude. Due to the diffusion of volcanic aerosols in the stratosphere and the advantages in laser energy of the DQ-1 system, the results from DQ-1 indicate a broader distribution  
360 range of volcanic aerosols. By August 1<sup>st</sup>, volcanic aerosols had extended southward to 50° S latitude, with an altitude of less than 20 km. From September to December, aerosols are consistently reduced and dissipated within 30° S to 60° S latitude. By December 1<sup>st</sup>, their distribution spanned from 30° S to 50° S latitude, decreasing altitudes to around 15 km.

#### 5 Conclusion

This research has studied satellite-based retrieval algorithms and multi-source data validation of algorithmic results to obtain  
365 satellite-based aerosol optical properties accurately. The aerosol optical parameters obtained from DQ-1 have been validated against the product of CALIPSO and molecular backscatter coefficients. The results indicated that DQ-1 exhibited a higher SNR and conforms to the results of trends in molecular scattering. Data products from MPLNET stations, representing the three underlying surface types, have been selected for satellite-to-ground validation purposes using DQ-1. Both datasets have yielded consistent trends in the depolarization ratio and backscatter coefficient profiles, with a relative error of 25% after  
370 excluding cloud interference. Comparing the AOD from DQ-1 with the AOD obtained from AERONET within the selected spatiotemporal domain, a correlation analysis has yielded a value of  $R^2$  0.803 and RMSE of 0.1231, indicating a strong correlation between the two datasets. The validation process, conducted in conjunction with CALIPSO, MPLNET, and

AERONET, has ensured the accuracy of the raw data and retrieval results obtained by the system. This paper has undertaken an initial application into the transport of dust aerosols in East Africa on the retrieval-based results. The research findings indicate that the lidar ratio remains constant during the aerosol transport process, while the depolarization ratio and backscatter coefficient are decreased. The study employed the attenuated backscatter coefficient from CALIPSO and DQ-1 to investigate the South Atlantic stratospheric volcanic aerosols in 2022. The research findings have unveiled the latitude and altitude variations in the vertical distribution of volcanic aerosols. The mentioned preliminary scientific applications demonstrate that the DQ-1 spaceborne HSRL system is capable of accurate global observations. The system can be used to obtain far more efficient retrieval techniques and comprehensive multi-source data validation with further scientific applications. Therefore, it can be a suitable alternative for satellite-based systems like CALIPSO. The above preliminary scientific applications demonstrate that the HSRL system is capable of accurate global observations.

### **Data availability**

The DQ-1 L2A data was not publicly available at the time our manuscript was submitted. We were able to access the data by joining as part of the scientific team for DQ-1. The ERA5 dataset is downloaded via the website <https://cds.climate.copernicus.eu/> (last access: 10 October 2023). The AERONET dataset is downloaded via the website <https://aeronet.gsfc.nasa.gov/> (last access: 10 October 2023). The MPLNET dataset is downloaded via the website <https://mplnet.gsfc.nasa.gov/> (last access: 10 October 2023). The CALIPSO dataset is downloaded via the website <https://asdc.larc.nasa.gov/project/CALIPSO/> (last access: 10 October 2023).

### **Author contributions**

C. Zha contributed to algorithm development and data analysis and wrote the manuscript. L. Bu, Q. Wang contributed to scientific discussions and reviewed the manuscript. A. Mubarak and P. Liyanage contributed to modifying the grammar of the manuscript and reviewed the manuscript. All the co-authors reviewed and edited the manuscript.

### **Competing interests**

The authors declare that they have no conflict of interest.

### **Acknowledgments**

We thank the Shanghai Institute of Optics and Fine Mechanics, Chinese Academy of Sciences for providing the Level 2A data of DQ-1. We thank the AERONET Principal Investigators and their staff for establishing and maintaining the AERONET at the 40 sites used in this work. We thank NASA Langley Research Center for providing the data sets of CALIPSO. We are also

400 thankful to the MPLNET PIs for their effort in establishing and maintaining the Apalachin, El Arenosillo, and Santa Cruz Tenerife sites. We also thank the European Centre for Medium-Range Weather Forecasts (ECMWF) for providing the ERA5 dataset.

This research was funded by the National Natural Science Foundation of China (Grant No. 42175145) and the Shanghai Aerospace Science and Technology Innovation Foundation (SAST2022-039).

## 405 **References**

Abril-Gago, J., Guerrero-Rascado, J. L., Costa, M. J., Bravo-Aranda, J. A., Sicard, M., Bermejo-Pantaleón, D., Bortoli, D., Granados-Muñoz, M. J., Rodríguez-Gómez, A., Muñoz-Porcar, C., Comerón, A., Ortiz-Amezcuca, P., Salgueiro, V., Jiménez-Martín, M. M., and Alados-Arboledas, L.: Statistical validation of Aeolus L2A particle backscatter coefficient retrievals over ACTRIS/EARLINET stations on the Iberian Peninsula, *Atmos. Chem. Phys.*, 22, 1425-1451, 10.5194/acp-22-1425-2022, 410 2022.

Bibi, H., Alam, K., Chishtie, F., Bibi, S., Shahid, I., and Blaschke, T.: Intercomparison of MODIS, MISR, OMI, and CALIPSO aerosol optical depth retrievals for four locations on the Indo-Gangetic plains and validation against AERONET data, *Atmospheric Environment*, 111, 113-126, <https://doi.org/10.1016/j.atmosenv.2015.04.013>, 2015.

Burton, S. P., Ferrare, R. A., Hostetler, C. A., Hair, J. W., Rogers, R. R., Obland, M. D., Butler, C. F., Cook, A. L., Harper, D. B., and Froyd, K. D.: Aerosol classification using airborne High Spectral Resolution Lidar measurements – methodology and 415 examples, *Atmos. Meas. Tech.*, 5, 73-98, 10.5194/amt-5-73-2012, 2012a.

Burton, S. P., Ferrare, R. A., Omar, A. H., Hostetler, C. A., Hair, J. W., Rogers, R., Obland, M. D., Butler, C. F., Cook, A. L., and Harper, D. B.: Comparison of Aerosol Classification from Airborne High Spectral Resolution Lidar and the CALIPSO Vertical Feature Mask, December 01, 20122012b.

420 The Cloud-Aerosol Lidar and Infrared Pathfinder Satellite Observation (CALIPSO): <https://www-calipso.larc.nasa.gov/>, last access: Jan 2nd.

Changzhe, D., Juan, Z., Xinyu, S., Jinru, Y., Fengyang, W., Yang, Z., Juxin, Y., and Zhenyang, L.: Design and Verification for DQ-1 Satellite Aerial Experiment, *Aerospace Shanghai (Chinese & English)*, 40, 122-131, 10.19328/j.cnki.2096-8655.2023.03.015, 2023.

425 Chiang, C.W., Kumar Das, S., Shih, Y.F., Liao, H.S., and Nee, J.B.: Comparison of CALIPSO and ground-based lidar profiles over Chung-Li, Taiwan, *Journal of Quantitative Spectroscopy and Radiative Transfer*, 112, 197-203, <https://doi.org/10.1016/j.jqsrt.2010.05.002>, 2011.

Cornut, F., Amraoui, L., Cuesta, J., and Blanc, J.: Added Value of Aerosol Observations of a Future AOS High Spectral Resolution Lidar with Respect to Classic Backscatter Spaceborne Lidar Measurements, *Remote Sensing*, 15, 506, 430 10.3390/rs15020506, 2023.

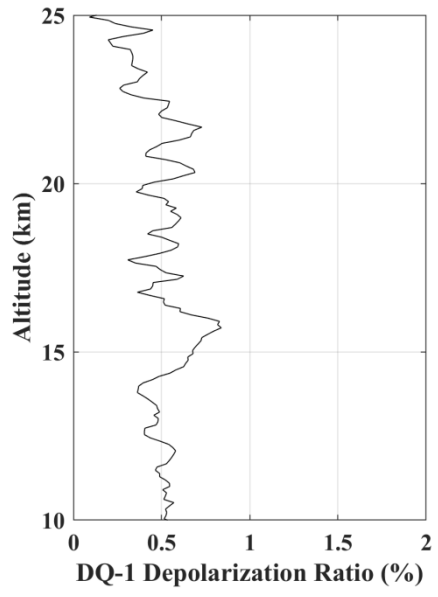
- Crawford, A. M., Stunder, B. J. B., Ngan, F., and Pavolonis, M. J.: Initializing HYSPLIT with satellite observations of volcanic ash: A case study of the 2008 Kasatochi eruption, *Journal of Geophysical Research: Atmospheres*, 121, 10,786-710,803, <https://doi.org/10.1002/2016JD024779>, 2016.
- 435 Dai, G., Wu, S., Long, W., Liu, J., Xie, Y., Sun, K., Meng, F., Song, X., Huang, Z., and Chen, W.: Aerosols and Clouds data processing and optical properties retrieval algorithms for the spaceborne ACDL/DQ-1, *EGUsphere*, 2023, 1-20, 10.5194/egusphere-2023-2182, 2023.
- Dong, J., Liu, J., Zhu, X., Bi, D., Zhu, X., and Chen, W.: Splitting ratio optimization of spaceborne high spectral resolution lidar, *Infrared and Laser Engineering*, 48, 7-12, 10.3788/IRLA201948.S205001, 2019.
- 440 Dong, J., Liu, J., Bi, D., Ma, X., Zhu, X., Zhu, X., and Chen, W.: Optimal iodine absorption line applied for spaceborne high spectral resolution lidar, *Appl. Opt.*, 57, 5413-5419, 10.1364/AO.57.005413, 2018.
- Draxler, R. R. and Hess, G. D.: Description of the HYSPLIT4 modeling system, 1997.
- Esselborn, M., Wirth, M., Fix, A., Tesche, M., and Ehret, G.: Airborne high spectral resolution lidar for measuring aerosol extinction and backscatter coefficients, *Appl Opt*, 47, 346-358, 10.1364/ao.47.000346, 2008.
- 445 Getzewich, B. J., Vaughan, M. A., Hunt, W. H., Avery, M. A., Powell, K. A., Tackett, J. L., Winker, D. M., Kar, J., Lee, K. P., and Toth, T. D.: CALIPSO lidar calibration at 532 nm: version 4 daytime algorithm, *Atmos. Meas. Tech.*, 11, 6309-6326, 10.5194/amt-11-6309-2018, 2018.
- Groß, S., Esselborn, M., Weinzierl, B., Wirth, M., Fix, A., and Petzold, A.: Aerosol classification by airborne high spectral resolution lidar observations, *Atmos. Chem. Phys.*, 13, 2487-2505, 10.5194/acp-13-2487-2013, 2013.
- 450 Groß, S., Tesche, M., Freudenthaler, V., Toledano, C., Wiegner, M., Ansmann, A., Althausen, D., and Seefeldner, M.: Characterization of Saharan dust, marine aerosols and mixtures of biomass-burning aerosols and dust by means of multi-wavelength depolarization and Raman lidar measurements during SAMUM 2, *Tellus B*, 63, 706-724, <https://doi.org/10.1111/j.1600-0889.2011.00556.x>, 2011.
- 455 Guibert, S., Matthias, V., Schulz, M., Bösenberg, J., Eixmann, R., Mattis, I., Pappalardo, G., Rita Perrone, M., Spinelli, N., and Vaughan, G.: The vertical distribution of aerosol over Europe—synthesis of one year of EARLINET aerosol lidar measurements and aerosol transport modeling with LMDzT-INCA, *Atmospheric Environment*, 39, 2933-2943, <https://doi.org/10.1016/j.atmosenv.2004.12.046>, 2005.
- Hair, J. W., Caldwell, L. M., Krueger, D. A., and She, C.-Y.: High-Spectral-Resolution Lidar with Iodine-Vapor Filters: Measurement of Atmospheric-State and Aerosol Profiles, *Appl. Opt.*, 40, 5280-5294, 10.1364/AO.40.005280, 2001.
- 460 Holben, B. N., Eck, T. F., Slutsker, I., Tanré, D., Buis, J. P., Setzer, A., Vermote, E., Reagan, J. A., Kaufman, Y. J., Nakajima, T., Lavenu, F., Jankowiak, I., and Smirnov, A.: AERONET—A Federated Instrument Network and Data Archive for Aerosol Characterization, *Remote Sensing of Environment*, 66, 1-16, [https://doi.org/10.1016/S0034-4257\(98\)00031-5](https://doi.org/10.1016/S0034-4257(98)00031-5), 1998.
- Huang, J., Minnis, P., Chen, B., Huang, Z., Liu, Z., Zhao, Q., Yi, Y., and Ayers, J. K.: Long-range transport and vertical structure of Asian dust from CALIPSO and surface measurements during PACDEX, *Journal of Geophysical Research: Atmospheres*, 113, <https://doi.org/10.1029/2008JD010620>, 2008.

- 465 Juxin, Y., Yang, Z., Chuncan, F., Qin, W., Xufeng, Z., Shiguang, L., Junxuan, Z., Lingbing, B., Jiqiao, L., and Weibiao, C.: Development and Flight Verification of Airborne Aerosol and Carbon Dioxide Detection Lidar, *Aerospace Shanghai* (Chinese & English), 40, 84-92, 10.19328/j.cnki.2096-8655.2023.03.010, 2023.
- Kaufman, Y. J., Tanré, D., and Boucher, O.: A satellite view of aerosols in the climate system, *Nature*, 419, 215-223, 10.1038/nature01091, 2002.
- 470 Ke, J., Sun, Y., Dong, C., Zhang, X., Wang, Z., Lyu, L., Zhu, W., Ansmann, A., Su, L., Bu, L., Xiao, D., Wang, S., Chen, S., Liu, J., Chen, W., and Liu, D.: Development of China's first space-borne aerosol-cloud high-spectral-resolution lidar: retrieval algorithm and airborne demonstration, *PhotonIX*, 3, 17, 10.1186/s43074-022-00063-3, 2022.
- Knobelspiesse, K., Cairns, B., Ottaviani, M., Ferrare, R., Hair, J., Hostetler, C., Obland, M., Rogers, R., Redemann, J., Shinozuka, Y., Clarke, A., Freitag, S., Howell, S., Kapustin, V., and McNaughton, C.: Combined retrievals of boreal forest  
475 fire aerosol properties with a polarimeter and lidar, *Atmos. Chem. Phys.*, 11, 7045-7067, 10.5194/acp-11-7045-2011, 2011.
- Langley Research Center. *The Cloud-Aerosol Lidar and Infrared Pathfinder Satellite Observation (CALIPSO)*. <https://www-calipso.larc.nasa.gov/>
- Liu, D., Zheng, Z., Chen, W., Wang, Z., Li, W., Ke, J., Zhang, Y., Chen, S., Cheng, C., and Wang, S.: Performance estimation of space-borne high-spectral-resolution lidar for cloud and aerosol optical properties at 532 nm, *Opt Express*, 27, A481-a494,  
480 10.1364/oe.27.00a481, 2019a.
- Liu, Z., Kar, J., Zeng, S., Tackett, J., Vaughan, M., Avery, M., Pelon, J., Getzewich, B., Lee, K. P., Magill, B., Omar, A., Lucker, P., Trepte, C., and Winker, D.: Discriminating between clouds and aerosols in the CALIOP version 4.1 data products, *Atmos. Meas. Tech.*, 12, 703-734, 10.5194/amt-12-703-2019, 2019b.
- Mattis, I., Ansmann, A., Müller, D., Wandinger, U., and Althausen, D.: Multiyear aerosol observations with dual-wavelength  
485 Raman lidar in the framework of EARLINET, *Journal of Geophysical Research: Atmospheres*, 109, <https://doi.org/10.1029/2004JD004600>, 2004.
- McGill, M. J., Vaughan, M. A., Trepte, C. R., Hart, W. D., Hlavka, D. L., Winker, D. M., and Kuehn, R.: Airborne validation of spatial properties measured by the CALIPSO lidar, *Journal of Geophysical Research: Atmospheres*, 112, <https://doi.org/10.1029/2007JD008768>, 2007.
- 490 McPherson, C. J., Reagan, J. A., Schafer, J., Giles, D., Ferrare, R., Hair, J., and Hostetler, C.: AERONET, airborne HSRL, and CALIPSO aerosol retrievals compared and combined: A case study, *Journal of Geophysical Research: Atmospheres*, 115, <https://doi.org/10.1029/2009JD012389>, 2010.
- Nishizawa, T., Sugimoto, N., Matsui, I., Shimizu, A., Higurashi, A., and Jin, Y.: The Asian Dust and Aerosol Lidar Observation Network (AD-NET): Strategy and Progress, *EPJ Web of Conferences*, 119, 19001, 2016.
- 495 Omar, A. H., Winker, D. M., Tackett, J. L., Giles, D. M., Kar, J., Liu, Z., Vaughan, M. A., Powell, K. A., and Trepte, C. R.: CALIOP and AERONET aerosol optical depth comparisons: One size fits none, *Journal of Geophysical Research: Atmospheres*, 118, 4748-4766, <https://doi.org/10.1002/jgrd.50330>, 2013.



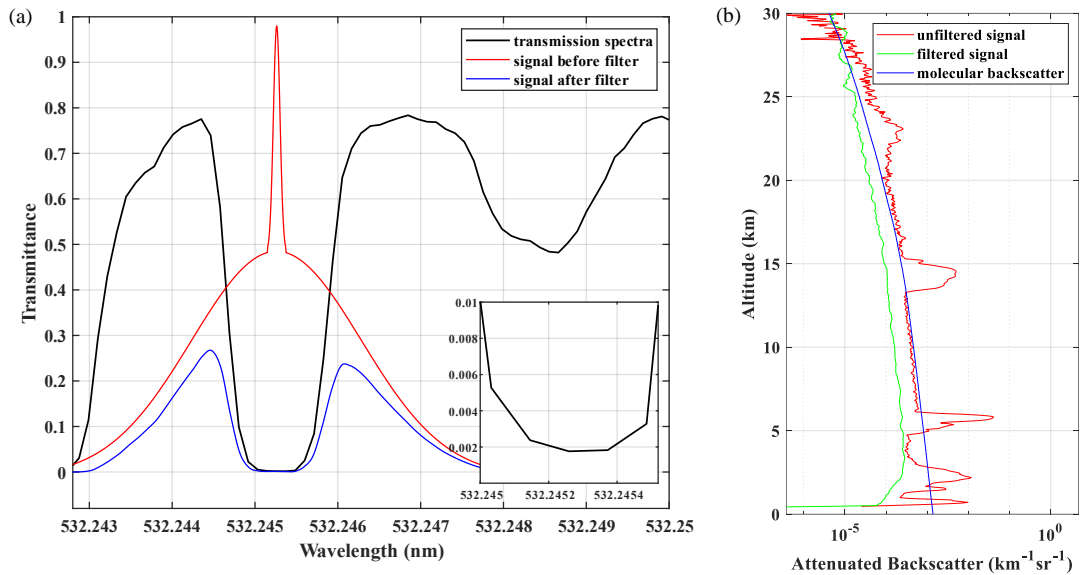
- Pappalardo, G., Amodeo, A., Apituley, A., Comeron, A., Freudenthaler, V., Linné, H., Ansmann, A., Bösenberg, J., D'Amico, G., Mattis, I., Mona, L., Wandinger, U., Amiridis, V., Alados-Arboledas, L., Nicolae, D., and Wiegner, M.: EARLINET: towards an advanced sustainable European aerosol lidar network, *Atmos. Meas. Tech.*, 7, 2389-2409, 10.5194/amt-7-2389-2014, 2014.
- Pitari, G., Di Carlo, P., Coppari, E., De Luca, N., Di Genova, G., Iarlori, M., Pietropaolo, E., Rizi, V., and Tuccella, P.: Aerosol measurements at L'Aquila EARLINET station in central Italy: Impact of local sources and large scale transport resolved by LIDAR, *Journal of Atmospheric and Solar-Terrestrial Physics*, 92, 116-123, <https://doi.org/10.1016/j.jastp.2012.11.004>, 2013.
- Proestakis, E., Amiridis, V., Marinou, E., Biniotoglou, I., Ansmann, A., Wandinger, U., Hofer, J., Yorks, J., Nowottnick, E., Makhmudov, A., Papayannis, A., Pietruczuk, A., Gialitaki, A., Apituley, A., Szkop, A., Muñoz Porcar, C., Bortoli, D., Dionisi, D., Althausen, D., Mamali, D., Balis, D., Nicolae, D., Tetoni, E., Liberti, G. L., Baars, H., Mattis, I., Stachlewska, I. S., Voudouri, K. A., Mona, L., Mylonaki, M., Perrone, M. R., Costa, M. J., Sicard, M., Papagiannopoulos, N., Siomos, N., Burlizzi, P., Pauly, R., Engelmann, R., Abdullaev, S., and Pappalardo, G.: EARLINET evaluation of the CATS Level 2 aerosol backscatter coefficient product, *Atmos. Chem. Phys.*, 19, 11743-11764, 10.5194/acp-19-11743-2019, 2019.
- Qin, K., Wu, L., Wong, M. S., Letu, H., Hu, M., Lang, H., Sheng, S., Teng, J., Xiao, X., and Yuan, L.: Trans-boundary aerosol transport during a winter haze episode in China revealed by ground-based Lidar and CALIPSO satellite, *Atmospheric Environment*, 141, 20-29, <https://doi.org/10.1016/j.atmosenv.2016.06.042>, 2016.
- Reverdy, M., Chepfer, H., Donovan, D., Noel, V., Cesana, G., Hoareau, C., Chiriaco, M., and Bastin, S.: An EarthCARE/ATLID simulator to evaluate cloud description in climate models, *Journal of Geophysical Research: Atmospheres*, 120, 11,090-011,113, <https://doi.org/10.1002/2015JD023919>, 2015.
- Stein, A. F., Draxler, R. R., Rolph, G. D., Stunder, B. J. B., Cohen, M. D., and Ngan, F.: NOAA's HYSPLIT Atmospheric Transport and Dispersion Modeling System, *Bulletin of the American Meteorological Society*, 96, 2059-2077, <https://doi.org/10.1175/BAMS-D-14-00110.1>, 2015.
- Tenti, G., Boley, C. D., and Desai, R. C.: On the Kinetic Model Description of Rayleigh–Brillouin Scattering from Molecular Gases, *Canadian Journal of Physics*, 52, 285-290, 10.1139/p74-041, 1974.
- Tesche, M., A. Ansmann, D. Müller, D. Althausen, R. Engelmann, V. Freudenthaler, and S. Groß: Vertically resolved separation of dust and smoke over Cape Verde using multiwavelength Raman and polarization lidars during Saharan Mineral Dust Experiment 2008, *J. Geophys. Res.*, 114, D13202, doi:10.1029/2009JD011862.
- Vaughan, M., Garnier, A., Josset, D., Avery, M., Lee, K. P., Liu, Z., Hunt, W., Pelon, J., Hu, Y., Burton, S., Hair, J., Tackett, J. L., Getzewich, B., Kar, J., and Rodier, S.: CALIPSO lidar calibration at 1064 nm: version 4 algorithm, *Atmos. Meas. Tech.*, 12, 51-82, 10.5194/amt-12-51-2019, 2019.
- Wang, Q., Bu, L., Tian, L., Xu, J., Zhu, S., and Liu, J.: Validation of an airborne high spectral resolution Lidar and its measurement for aerosol optical properties over Qinhuangdao, China, *Opt Express*, 28, 24471-24488, 10.1364/oe.397582, 2020.

- Wang, T., Fetzer, E. J., Wong, S., Kahn, B. H., and Yue, Q.: Validation of MODIS cloud mask and multilayer flag using CloudSat-CALIPSO cloud profiles and a cross-reference of their cloud classifications, *Journal of Geophysical Research: Atmospheres*, 121, 11,620-611,635, <https://doi.org/10.1002/2016JD025239>, 2016.
- Wang, X. and Chen, J.: Fog Formation in Cold Season in Ji'nan, China: Case Analyses with Application of HYSPLIT Model, *Advances in Meteorology*, 2014, 940956, 10.1155/2014/940956, 2014.
- Wehr, T., Kubota, T., Tzeremes, G., Wallace, K., Nakatsuka, H., Ohno, Y., Koopman, R., Rusli, S., Kikuchi, M., Eisinger, M., Tanaka, T., Taga, M., Deghaye, P., Tomita, E., and Bernaerts, D.: The EarthCARE mission – science and system overview, *Atmos. Meas. Tech.*, 16, 3581-3608, 10.5194/amt-16-3581-2023, 2023.
- Weibiao, C., Jiqiao, L., Xia, H., Huaguo, Z., Xiuhua, M., Yuan, W., and Xiaopeng, Z.: Lidar Technology for Atmosphere Environment Monitoring Satellite, *Aerospace Shanghai (Chinese & English)*, 40, 13-20, 10.19328/j.cnki.2096-8655.2023.03.002, 2023.
- Welton, E., Campbell, J., Spinhirne, J., and Scott, V. S.: Global monitoring of clouds and aerosols using a network of micropulse lidar systems, *Second International Asia-Pacific Symposium on Remote Sensing of the Atmosphere, Environment, and Space, SPIE2001*.
- Winker, D., Pelon, J., Jr, J., Ackerman, S., Charlson, R., Colarco, P., Flamant, P., Fu, Q., Hoff, R., Kittaka, C., Kubar, T., Treut, H., McCormick, M., Mégie, G., Poole, L., Trepte, C., Vaughan, M., and Wielicki, B.: The Calipso Mission: A Global 3D View of Aerosols and Clouds, *Bulletin of the American Meteorological Society*, 91, 10.1175/2010BAMS3009.1, 2010.
- Xiong, Z., Xu, X., Yang, Y., and Luo, T.: Diurnal vertical distribution and transport of dust aerosol over and around Tibetan Plateau from lidar on International Space Station, *Atmospheric Research*, 106939, <https://doi.org/10.1016/j.atmosres.2023.106939>, 2023.
- Xu, J., Bu, L., Liu, J., Zhang, Y., Zhu, S., Wang, Q., Zhu, X., and Chen, W.: Airborne High-Spectral-Resolution Lidar for Atmospheric Aerosol Detection, *Chinese Journal of Lasers*, 47, 411-420, 10.3788/CJL202047.0710003, 2020.
- Yorks, J. E., McGill, M. J., Palm, S. P., Hlavka, D. L., Selmer, P. A., Nowotnick, E. P., Vaughan, M. A., Rodier, S. D., and Hart, W. D.: An overview of the CATS level 1 processing algorithms and data products, *Geophysical Research Letters*, 43, 4632-4639, <https://doi.org/10.1002/2016GL068006>, 2016.
- Yufeng, H., Zhenhong, L., Le, W., Bo, C., Wu, Z., Shuangcheng, Z., Jiantao, D., Xuesong, Z., Jing, Y., Meiling, Z., Zhenjiang, L., Sisi, W., Chen, M., Lianchong, Z., and Jianbing, P.: Rapid Interpretation and Analysis of the 2022 Eruption of Hunga Tonga Hunga Ha'apai Volcano with Integrated Remote Sensing Techniques, *Geomatics and Information Science of Wuhan University*, 47, 242-250, 10.13203/j.whugis20220050, 2022.
- Zheng, Z., Chen, W., Zhang, Y., Chen, S., and Liu, D.: Denoising the space-borne high-spectral-resolution lidar signal with block-matching and 3D filtering, *Appl. Opt.*, 59, 2820-2828, 10.1364/AO.385469, 2020.
- Zhu, S., Bu, L., Liu, J., Wang, Q., Yang, J., Zhang, Y., Zhu, X., and Cheng, W.: Study on Airborne High Spectral Resolution Lidar Detecting Optical properties and Pollution of Atmospheric Aerosol, *Chinese Journal of Lasers*, 48, 164-176, 10.3788/CJL202148.1710003, 2021.



565

Figure 1 Retrieval results of depolarization ratio at high altitude.



570 Figure 2 The transmittance spectra of the filter and comparison of signals before and after filtering. (a) The actual measured  
transmittance spectra of the onboard iodine vapor filter of the DQ-1 satellite, the subfigure in the lower right corner display the  
transmittance spectrum in the 1110 line. The red solid line delineates the spectral of the echo signal prior to the filter (parallel  
channel), the blue solid line delineates the spectral of the echo signal after the filter (high spectral resolution channel). (b) Comparison  
of signals before and after filtering, the red line represents the unfiltered signal, the green line represents the filtered signal, and the  
575 blue line represents the molecular backscatter signal.

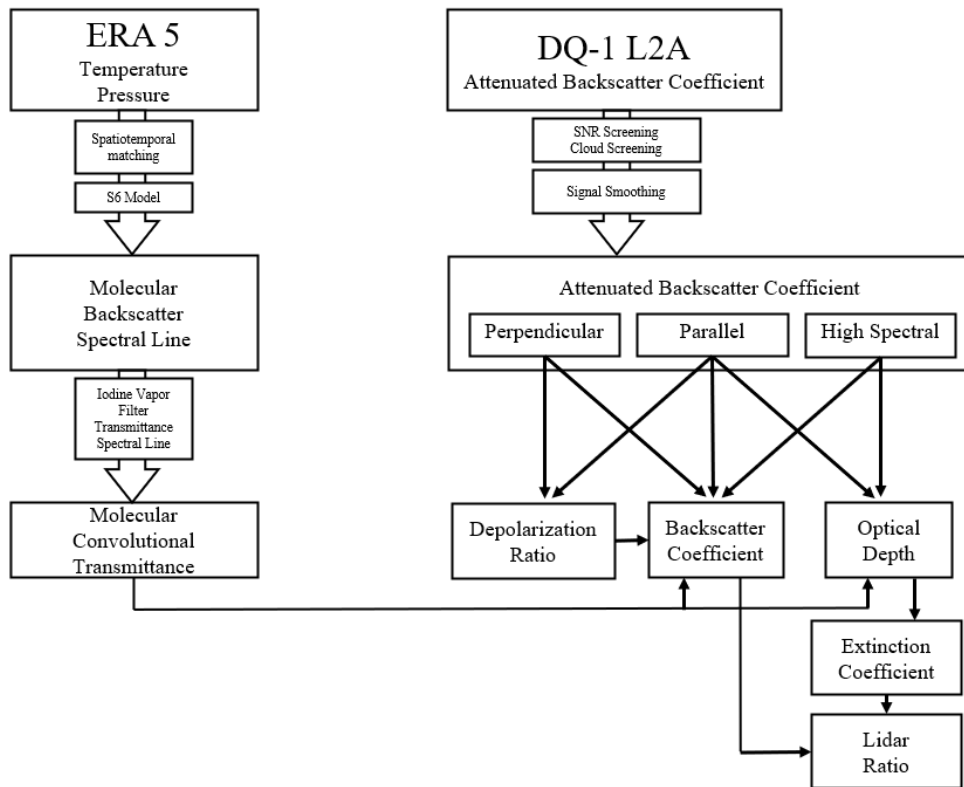
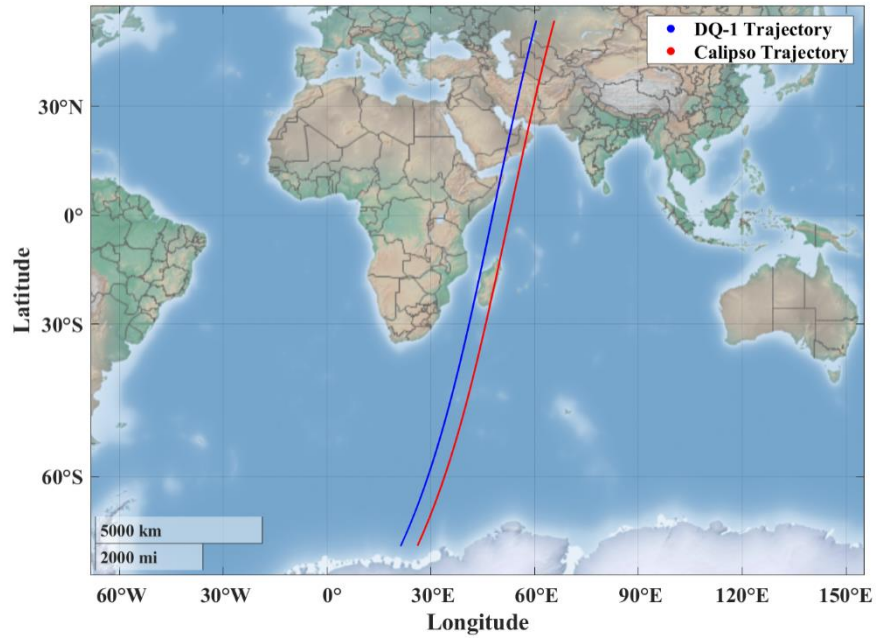
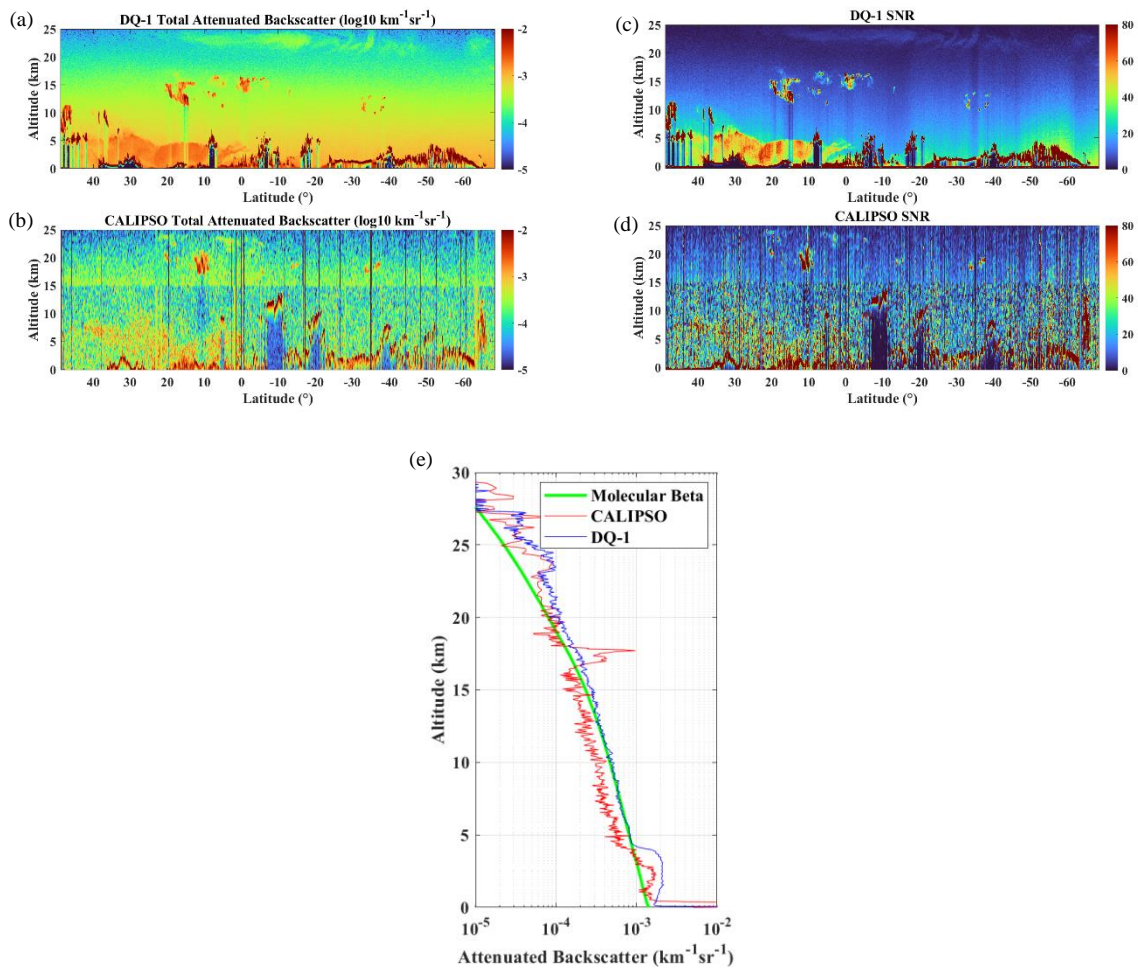


Figure 3 Flowchart of the DQ-1 retrieval algorithm

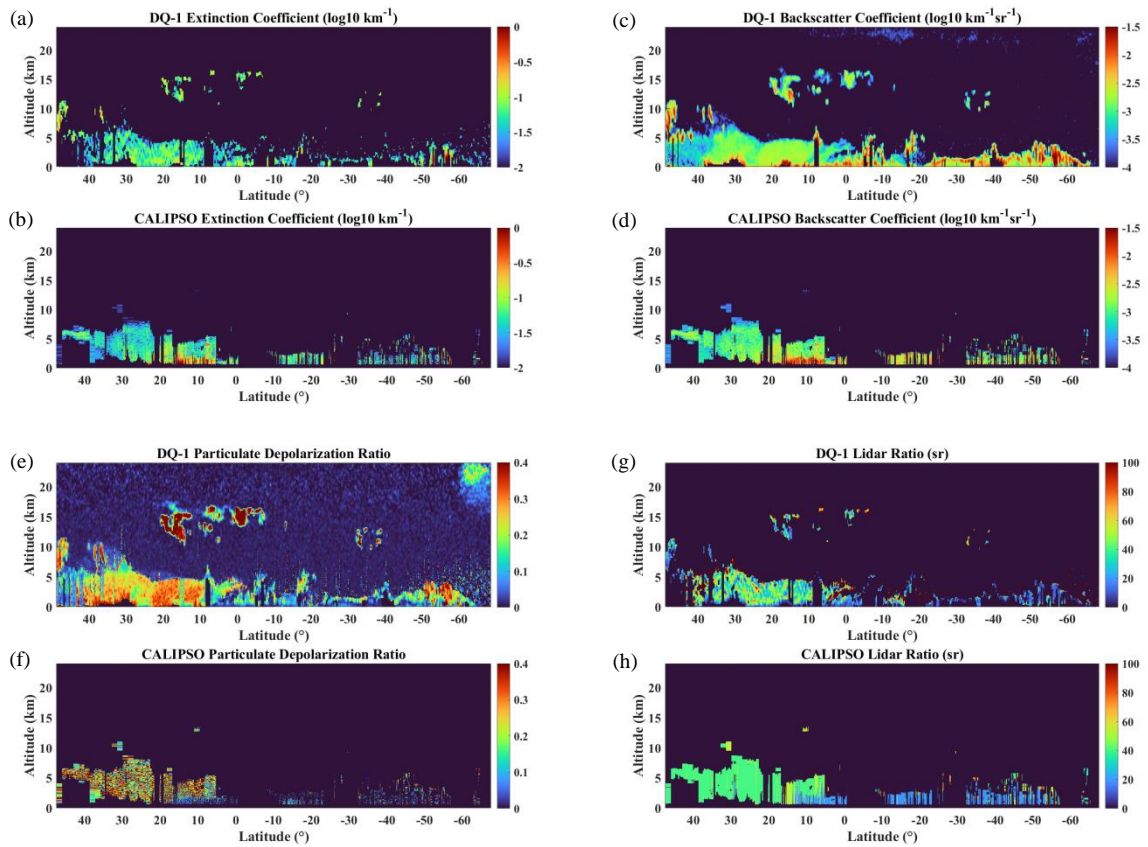
580



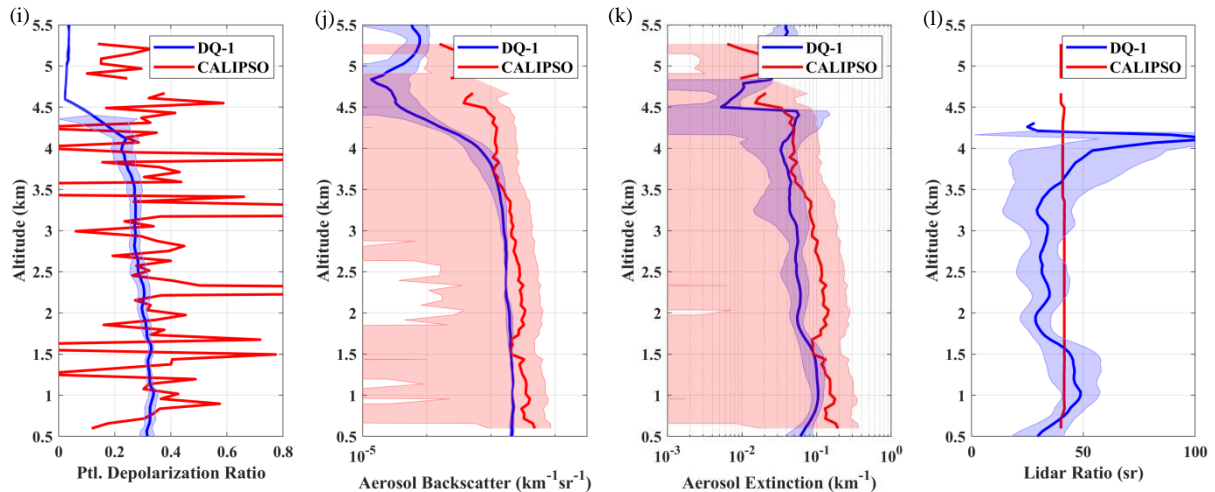
585 **Figure 4** The selected satellite trajectory of DQ-1 and CALIPSO in June 6, 2022. The DQ-1 trajectory is indicated by the blue solid line, while the CALIPSO trajectory is represented by the red solid line. Time difference between the two trajectories is 60 minutes, spatial separation amounts to 400 kilometers.



590 **Figure 5 Profile comparison of DQ-1 and CALIPSO on June 6, 2022: (a) Total attenuated backscatter coefficient profiles obtained by the DQ-1; (b) Total attenuated backscatter coefficient profiles obtained by the CALIPSO; (c) SNR of DQ-1 total attenuated backscatter; (d) SNR of CALIPSO total attenuated backscatter; (e) Comparison of total attenuated backscatter mean profile of 20° N to 22° N, the blue solid line represents the DQ-1 results, the red solid line represents the CALIPSO results, and the green solid line depicts the computed molecular backscatter coefficient.**



595



600

**Figure 6** Profile comparisons of DQ-1 and CALIPSO on June 6, 2022: (a) Extinction coefficient profiles of aerosols obtained by DQ-1; (b) Extinction coefficient profiles of aerosols obtained by CALIPSO; (c) Backscatter coefficient profiles of aerosols obtained by DQ-1; (d) Backscatter coefficient profiles of aerosols obtained by CALIPSO; (e) Particulate depolarization profile obtained by DQ-1; (f) Particulate depolarization profile obtained by CALIPSO; (g) Lidar ratio profile obtained by DQ-1; (h) Lidar ratio profile obtained by CALIPSO; (i) Comparison of particulate depolarization mean profile of 20°N to 22°N; (j) Comparison of aerosol



backscatter coefficient mean profile of 20°N to 22°N. (k) Comparison of aerosol extinction coefficient mean profile of 20°N to 22°N. (l) Aerosol lidar ratio profile of 20°N to 22°N. The blue solid line represents the DQ-1 results, the red solid line represents the CALIPSO results, the shaded area represents the standard deviation of different detection heights.

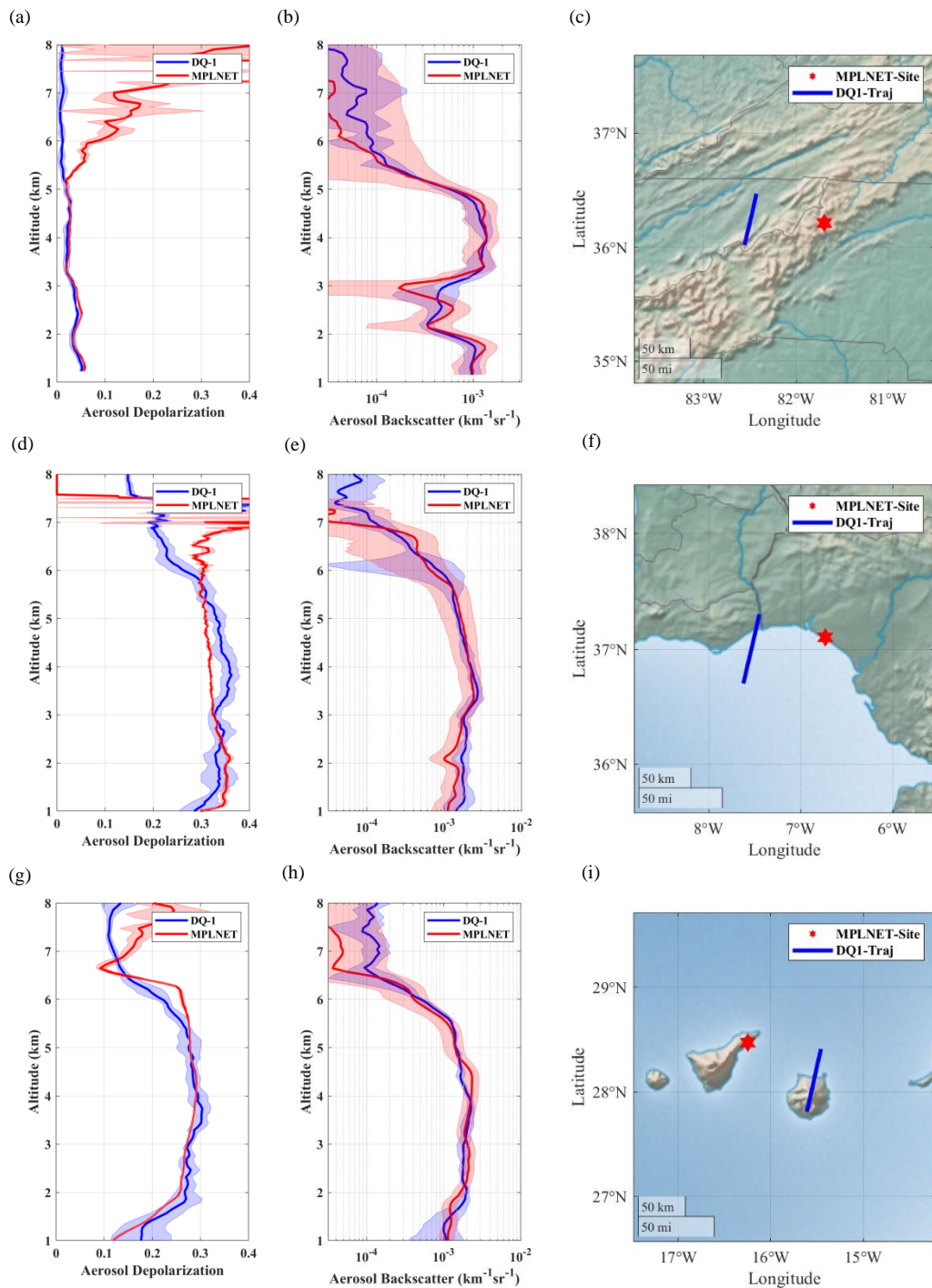
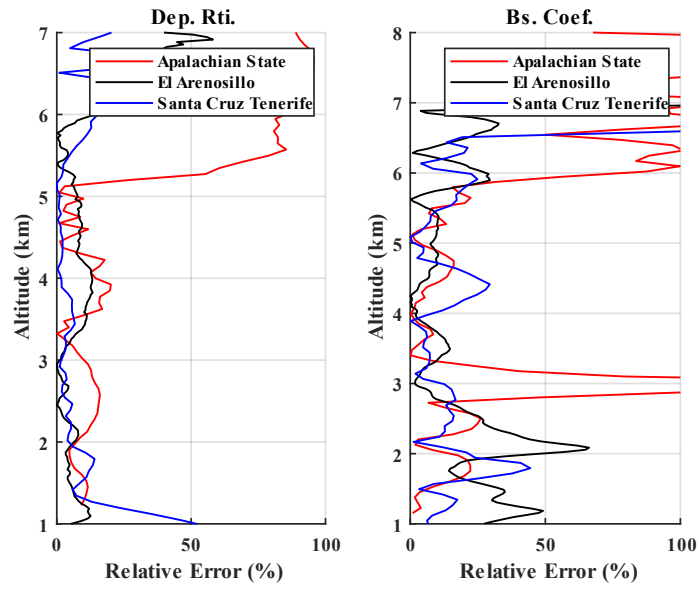
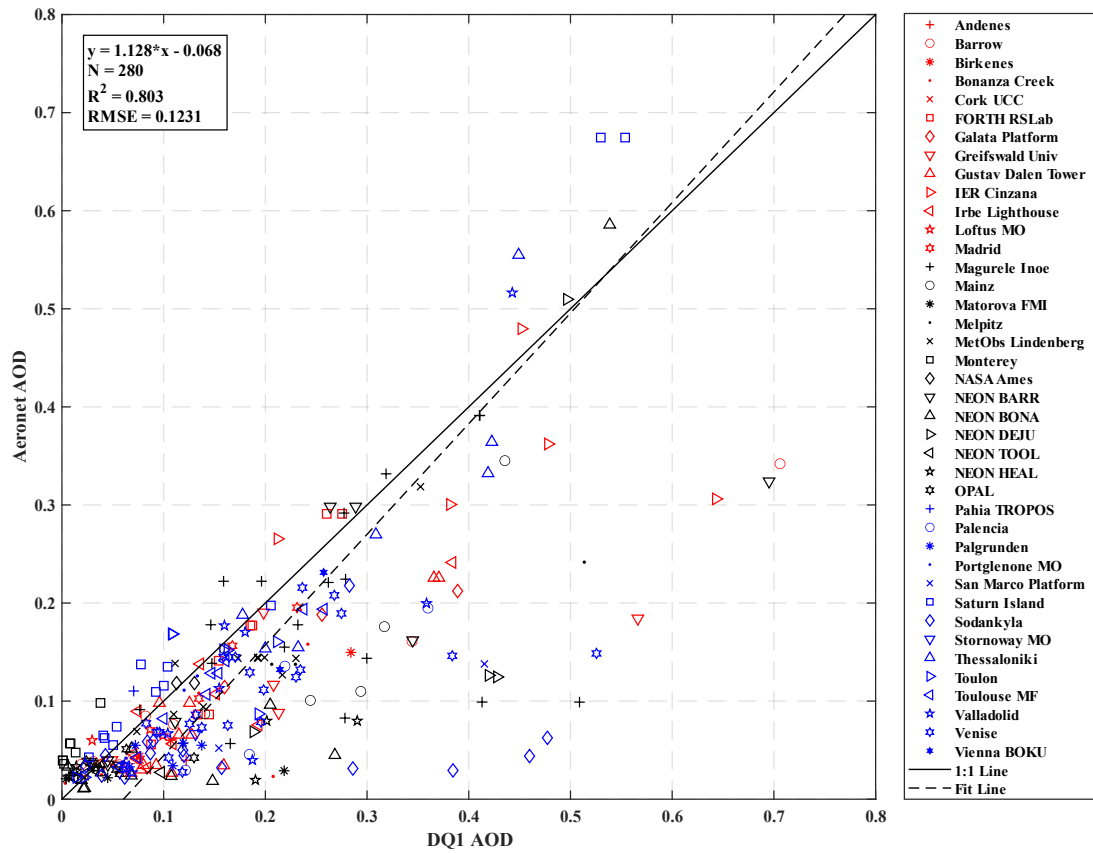


**Figure 7** Comparison of single profiles between DQ-1 and NASA MPLNET, The red solid line represents MPLNET results, blue solid line represents DQ-1 results, the shaded area represents the standard deviation of different altitudes. (a) Comparison of aerosol depolarization ratio profiles between DQ-1 and MPLNET Apalachin site on August 16, 2022; (b) Comparison of aerosol backscatter coefficient profiles between DQ-1 and MPLNET Apalachin site on August 16, 2022; (c) Trajectory of DQ-1 orbit and MPLNET Apalachin site location. (d) Comparison of aerosol depolarization ratio profiles between DQ-1 and MPLNET EL\_Arenosillo site on

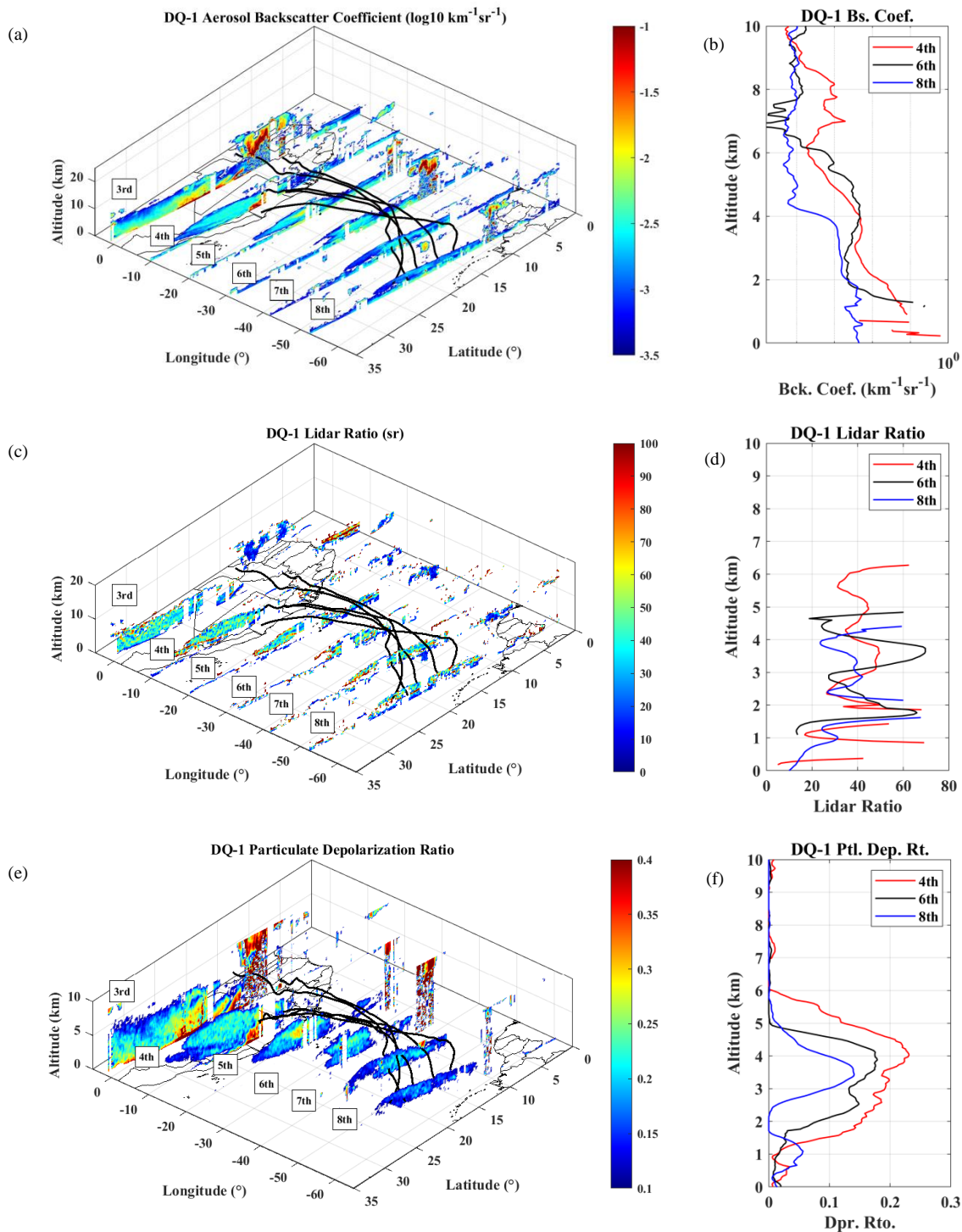
615 Jun 13, 2022; (e) Comparison of aerosol backscatter coefficient profiles between DQ-1 and MPLNET El\_Arenosillo site on Jun 13, 2022; (f) Trajectory of DQ-1 orbit and MPLNET El\_Arenosillo site location; (g) Comparison of aerosol depolarization ratio profiles between DQ-1 and MPLNET Santa\_Cruz\_Tenerife site on Aug 22, 2022; (h) Comparison of aerosol backscatter coefficient profiles between DQ-1 and MPLNET Santa\_Cruz\_Tenerife site on Aug 22, 2022; (i) Trajectory of DQ-1 orbit and MPLNET Santa\_Cruz\_Tenerife site location.



620 **Figure 8** The relative errors between the three MPL sites and DQ-1. The red line represents the relative error between the profiles of Apalachian State station and the DQ-1, the black line represents the relative error between the profiles of El Arenosillo station and the DQ-1, the blue line represents the relative error between the profiles of Santa Cruz Tenerife station and the DQ-1.



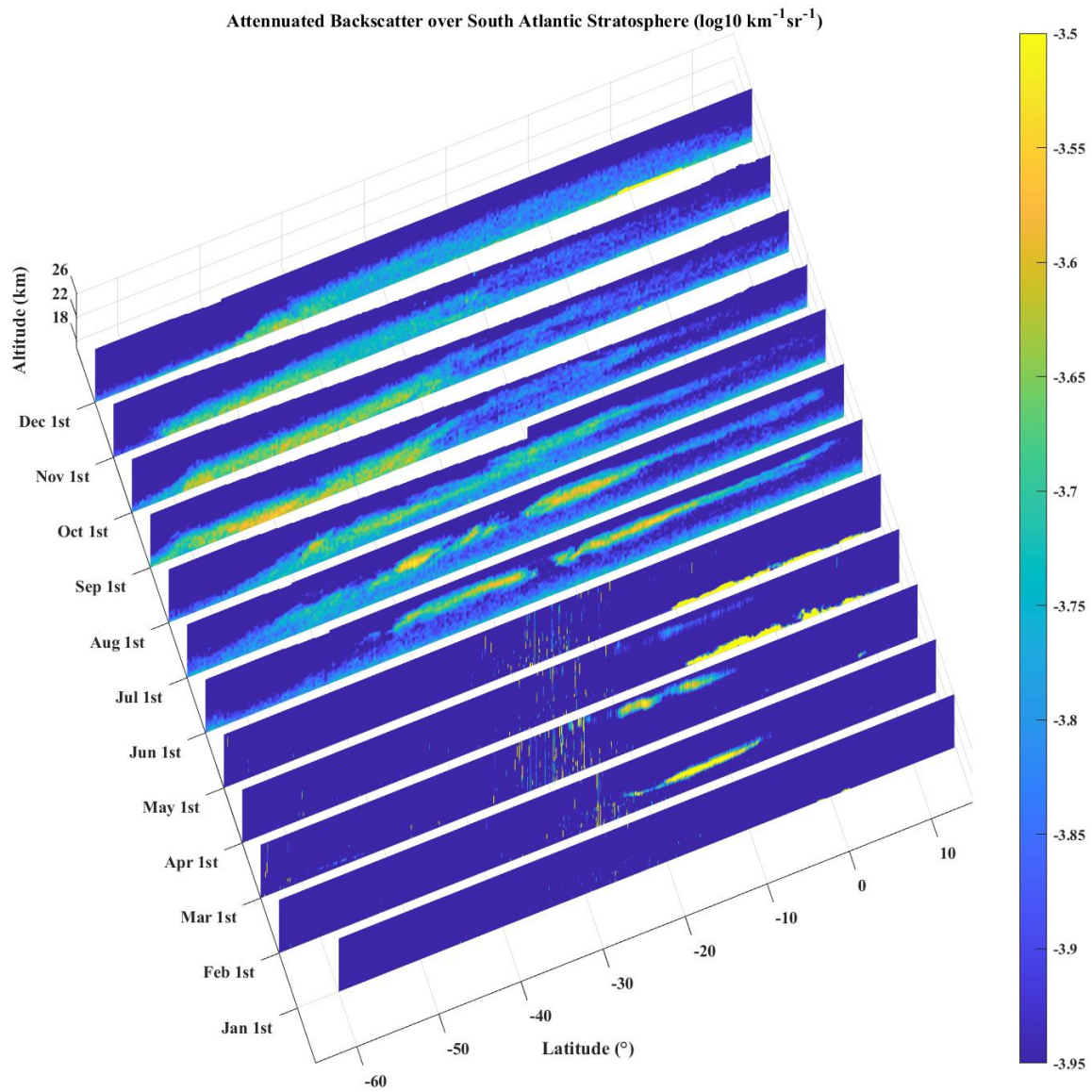
625 **Figure 9** Scatter plot of aerosol optical depth measured by DQ-1 and AERONET. Distinct shapes and colors are employed to indicate the scatter of AERONET and DQ-1 aerosol optical depth from various measurement sites. The solid black line represents the unity line (1:1), the black dashed line represents the outcome of a linear regression between the two datasets. The coefficient of determination (R-squared) is computed as 0.803, based on 280 fitted data points.



630

**Figure 10** Aerosol optical parameters retrieval results from DQ-1 over the Atlantic Ocean and corresponding HYSPLIT backward trajectory analysis. The figure presents observations from six orbits spanning July 3rd to July 8th, with dates indicated on the left side. The black solid lines denote the aerosol transport paths derived from the HYSPLIT backward trajectory analysis. (a) DQ-1

635 aerosol backscatter coefficient; (b) DQ-1 aerosol backscatter coefficient mean profile on the 4th, 6th and 8th; (c) DQ-1 lidar ratio; (d) DQ-1 lidar ratio mean profile on the 4th, 6th and 8th; (e) DQ-1 depolarization ratio (f) DQ-1 depolarization ratio mean profile on the 4th, 6th and 8th.



640 **Figure 11** Observed volcanic aerosol attenuated backscatter profile in the stratosphere over the South Atlantic in 2022. The left axis displays date, while the bottom axis displays latitude, with an altitude range of 18 to 26 km, displaying global information ng the observation results of a single orbit passing through the central South Pacific ( $10^\circ$  to  $30^\circ$  W) on the first day of each month. The results from January 1st to May 1st are derived from CALIPSO, while the results from June 1st to December 1st are derived from DQ-1.



**Table 1. Main parameters of the DQ-1 HSRL system (Dong et al., 2018; Weibiao et al., 2023).**

Parameter	Value
Laser Wavelength	532.245 nm
Laser Energy	$\geq 120$ mj for pulses A and B
Laser Frequency Stability	1MHz@10000s
Laser repetition frequency	40 Hz
Telescope aperture	1000 mm
Field of view	0.2 mrad
Broadband bandpass filter	0.45 nm
Narrowband FP filter	30 pm
HSRL filters	iodine vapor filter, 1110 line aerosol signal suppression ratio $\geq 25$ dB
Overall optical efficiency (excluding iodine filter)	0.16 at parallel polarized channel 0.561 at perpendicular polarized channel 0.375 at high spectral resolution channel
Quantum efficiency of the detector	40%
Retrieval result error	15%*

645 \* The relative error between the DQ-1 retrieval results (backscatter coefficient and depolarization ratio) and other authoritative data products, at low altitudes below 6 km under nighttime conditions.